Article

Metal−Organic Framework-Stabilized High Internal Phase Pickering Emulsions Based on Computer Simulation for Curcumin Encapsulation: Comprehensive Characterization and Stability Mechanism

Peihua Ma, Jinglin Zhang, Zi Teng, Yuan Zhang, Gary R. Bauchan, Yaguang Luo, Dongxia Liu, and Qin Wang*

Read Online

ACCESS | Metrics & More | Article Recommendations | SI Supporting Information

ABSTRACT: High internal phase Pickering emulsions (HIPPEs) have taken a center stage in the arena of delivery systems in the food industry because of their high loading capacity and stability. In addition, metal−organic frameworks (MOFs), a type of cutting-edge designable porous scaffolding material, have attracted attention in reticular chemistry, which satisfies fundamental demands for delivery research in the past years. Here, we demonstrate a novel metal−organic framework (MOF)-stabilized HIPPE delivery system for hydrophobic phytochemicals. First, a novel high-biocompatibility and stable MOF particle, UiO-66-NH$_2$, was selected from atomic simulation screening, which showed proper electronegativity and amphiphilic properties to develop the HIPPE system. Monodispersed UiO-66-NH$_2$ nanoparticles with the particle size of 161.36 nm were then prepared via solvothermal synthesization. Pickering emulsions with inner phase ratios from 50 to 80% with varied contents of polyethylene glycol (PEG) were prepared by in situ high-pressure homogenization, and their physicochemical properties including crystallography, morphology, and rheology were systematically characterized. Subsequently, curcumin, a model antioxidant, was loaded in the HIPPE system and named cur@UiO-66-NH$_2$/HIPPE. It exhibited high loading capacity, up to 6.93 ± 0.41%, and encapsulation efficiency (19.76 ± 3.84%). This novel MOF nanoparticle-stabilized HIPPE delivery system could be practically utilized for other bioactive components and antimicrobial agents, which would find applications in food safety and biomedical areas in the future.
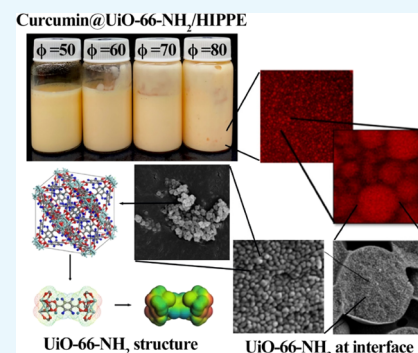
1. INTRODUCTION

There has been a breakthrough recently in the development of highly porous materials including, but not limited to, metal−organic frameworks (MOFs), zeolite, and covalent organic frameworks (COFs),[1] with MOFs attracting the most attention. As defined in the Cambridge Crystallographic Data Centre (CCDC) database, an MOF is a material "with a transition metal bonded to an oxygen or nitrogen atom via a polymeric bond".[2] In principle, all MOF crystalline structures share similar characteristics, such as tailorable pore sizes, high void fractions, and a large surface area. These unique properties have rendered MOFs with many applications, including chemical separation, gas storage, catalysis, drug delivery, imaging, 3D printing, biomolecule encapsulation, and batteries.[3] Until now, the research and applications of MOFs in the food field are still limited, mainly due to their instability in water and toxicological and cost considerations. However, the UiO-66 family, named from the University of Oslo, attracted attention since it has high thermal, chemical, water, and mechanical stability due to the strong bonds between the inorganic block and high coordination number (fcc lattices) in

the past decades. Also, it is worth noting that a rich number of studies have been published on UiO-66 toxicity in different cell lines, e.g., human lung epithelial cells (A549), human breast cancer cells (MCF-7), mouse alveolar macrophage cells (MH-S), mouse fibroblast cells (L929), and mouse photoreceptor cells (661W).[4−6] It was concluded that no acute toxicity was found when cellular uptake was less than 50 μg/mL for 24 h. In addition, the UiO-66 family was synthesized by terephthalic acid with zirconium salt, and the benzene ring could be effortlessly modified by different functional groups, such as −OH, −NH$_2$, −COOH, and −Br, which provides an opportunity to optimize the electronegativity and amphiphilic properties suitable for emulsion systems.[7,8] It has been applied to the preparation of pharmaceutical delivery systems, e.g.,

pulmonary drug delivery, pH-responsive drug delivery, and targeted drug delivery.

Pickering emulsions are 3D self-assembly systems that may be formed and stabilized by small organic or inorganic colloidal particles absorbing onto the interface of oil and water.[9] Many candidate particles can be applied to stabilize Pickering emulsions, including organic particles (e.g., protein) and inorganic particles (e.g., silica). The advantage of silica lies in its low cost and good stability. Previously, it was reported that lipid droplets coated with silica nanoparticles (NPs) decreased the rate of lipid digestion when compared with those coated with proteins.[10] However, emulsions stabilized by protein particles, e.g., zein, β-lactoglobulin, and kafirin,[11] have shown high biocompatibility and biodegradability, which appeals to consumers seeking clean labels for food products, but those emulsion systems had inferior stability and bioaccessibility compared to their silica-containing counterparts.[12] In addition to protein and silica, a broad range of colloidal particles has been applied recently for preparing Pickering emulsions, including graphene oxide (GO), microgels, cellulose, and chitin nanocrystals.[12,13] Due to toxicity and water instability concerns, only a few reports tried the MOF as a Pickering emulsion stabilizer, making it rather rare in the delivery system.

High internal phase Pickering emulsions (HIPPEs), also called gel emulsions, are a special kind of Pickering emulsion. In 1966, Lissant first defined the HIPPE system as one with a minimal internal phase volume ratio (ϕ) of the emulsion system of 0.7.[14] Now, HIPPEs are usually characterized by ϕ values higher than 0.64 for the random close packing and 0.74 for the close hexagonal packing.[15] HIPPEs have shown many special features, such as high physicochemical stability and high loading capacity, for encapsulated bioactives. Taking those advantages, HIPPEs have been used in various applications, including organic semiconductors, filter membranes, and drug delivery systems.[16] Several different theories explain the formation and stabilization of HIPPEs. In one theory, phase inversion was required for the formation of HIPPEs, possibly due to the involvement of the homogenization process that improved the uniformity of particles. In another theory, HIPPEs were stabilized by increasing the viscosity of the continuous phase or modifying the surface of colloids, which prevented the absorption of particles onto the interface and, thus, the formation of regular Pickering emulsions.[15] The third theory predicted that HIPPE systems were mechanically stabilized against phase inversion and sedimentation.[17]

Here, we reported the methodology of a computer simulation assistant to design a novel MOF HIPPE system and systematically evaluate the HIPPE system simultaneously, including its morphology, crystallography, morphology, and rheology. To explore the application of the MOF-HIPPE system in the food field, curcumin was encapsulated by the MOF-HIPPE system. Although this research was still in the early stage of introducing MOFs in food applications, the UiO-66-based HIPPE delivery system showed high stability and loading capability, representing a potential breakthrough in the food research area.

2. MATERIALS AND METHODS

2.1. Materials. Zirconium tetrachloride (99.5%), benzene-1,4-dicarboxylic acid (BDC, 98.0%), N,N-dimethylformamide (DMF, 99.0%), Nile red, polyethylene glycol (PEG, 10,000 kDa), curcumin (95%), and acetic acid (99.9%) were purchased from Sigma-Aldrich (St. Louis, MO, USA). All of the chemicals are in analytical grade.

2.2. Computational Calculation. Crystal structural units were downloaded from the Cambridge Crystallographic Data Center database (CCDC, https://www.ccdc.cam.ac.uk/). Because the unit-cell structures of Zr-based MOFs were very large, the structural units were reduced to eight-unit cells (2 × 2 × 2) in Material Studio (version 7.6). The molecular electrostatic potential maps of UiO-66 and UiO-66-NH$_2$ were performed by the density functional theory (DFT) method using the DMol^3 code. The DFT method in this code uses fast convergent three-dimensional numerical integration to calculate the electrostatic potential. Perdew−Wang 1991 (PW91) is a generalized gradient approximation (GGA)-level function and is considered as an adequate precision for this investigation.[18]

The crystal structure of UiO-66-NH$_2$ was calculated using the RASPA2 to obtain its mass and density.[19] The accessible pore volume, gravimetric surface area (nitrogen), geometric surface area, and window diameter were analyzed by pyWINDOW.[20]

The XRD pattern simulation was calculated by a simulation tool, VESTA, with a wave angle from 1° to 30°, and the relative intensity was set to 1.[8]

Grand canonical Monte Carlo (GCMC) simulations were used to calculate N$_2$ isotherms at 77 K for UiO-66 and UiO-66-NH$_2$. At each pressure, the parameter of the equilibration step at 10,000,000 was set as a computer ensemble average. The framework atom was taken from the Universal Force Field (UFF). A charge of −0.482 was placed on the N nuclei and that of +0.964 was placed at the center of mass. The Ewald and group summation method was used for all interactions with atom-based van der Waals. All calculations mentioned above were based on a sorption isotherm module in Materials Studio. Parameters mentioned above were taken from a previous study with some modifications.[21]

2.3. Synthesis of UiO-66-NH$_2$. UiO-66-NH$_2$ was synthesized by a solvothermal method according to a previous report with minor modification. First, ZrCl$_4$ (1.17 g, 5 mmol), 2-aminobenzene-1,4-dicarboxylic acid (NH$_2$-BDC) (0.90 g, 5 mmol), and acetic acid (1.0 mL) were dissolved in dimethylformamide (DMF) (30 mL) at room temperature. Then, the mixture was placed in a Teflon-lined stainless steel autoclave after adding 2 mL of deionized water and mixing completely. The autoclave was placed in an oven at 120 °C for 24 h. Afterward, the solution was cooled to room temperature for 30 min, and the resulting UiO-66-NH$_2$ particles were separated via centrifugation (12,096g, 10 min) at room temperature and washed three times with ethanol. The resulting white powder was dried in an oven for 4 h.[22]

2.4. Characterization of UiO-66-NH$_2$. *2.4.1. Crystal Structure.* X-ray powder diffraction (XRD) patterns were obtained from an XRD diffractometer (C2 Discover Bruker Diffractometer, Madison, WI, USA) with CuKα radiation to evaluate the crystal structure of the MOF. The X-ray scan ranged from (2θ) 3.5° to 30°, with a step size at 0.02°.[8,23]

2.4.2. Porosity and Surface Area. The porosity and surface area of the MOF were determined using an ASAP 2020 Physisorption Analyzer (Micromeritics Instrument Corporation, Norcross, GA, USA), following a previous study.[22] Sample tubes were cleaned ultrasonically and dried at 110 °C. The MOF samples were loaded into the sample tube for degassing for 24 h. The sample tube with MOFs was then

transferred to the analysis port with N_2 as the adsorptive gas and liquid nitrogen as the cold medium.[22] The nitrogen monolayer-saturated adsorption capacity and surface area were calculated following eqs 1 and 2, respectively

$$V_m = \frac{1}{A + I} \tag{1}$$

$$S_g = 4.325 \times V_m \tag{2}$$

where I is the slope of the adsorption isotherm fit line when P/P_0 is from 0.35 to 0.5, A is the intercept of the adsorption isotherm fit line when P/P_0 is from 0 h, V_m is the monolayer-adsorbed nitrogen quantity, and S_g is the BET surface area.

2.4.3. Thermal Analysis. Thermal analysis of the UiO-66-NH_2 samples was performed using a thermogravimetric analysis (TGA) instrument (2950, TA Instruments Inc., New Castle, DE). The parameters were modified from a previous study under a mixed air and N_2 flow of 100 mL min^{-1} (40% air, 60% N_2) with a heating rate of 10 K min^{-1} from 308 to 1073 K.[24]

2.4.4. Particle Size. Hydrodynamic diameters of UiO-66-NH_2 were measured by a dynamic light scattering (DLS) instrument (BI-200SM, Brookhaven Instruments Corp., Holtsville, NY), which was equipped with a 35 mW HeNe laser beam at a wavelength of 637 nm. All DLS measurements were performed three times at 25 °C.[25] Particle size determination was conducted by diluting the particle with deionized water to 1 mL to avoid multiple light scattering and the impact on the accuracy of the measurement.

2.4.5. Surface Charge. The electrophoretic mobility was determined at a pH range of 1.0 to 7.0 using a Zetasizer Nano ZS (Malvern Instruments, Worcestershire, UK). Each sample was measured three times in disposable folded capillary cells (DTS 1070, Malvern Instruments Ltd., Worcestershire, UK) at a particle concentration of 0.1 wt %, and at least 32 runs were performed per measurement.[25] The pH value was adjusted by adding HCl and NaOH dropwise and measured by a pH meter.

2.4.6. Morphology. A sample powder was dispersed onto ultrasmooth, round (12 mm-diameter) carbon adhesive tabs (Electron Microscopy Sciences, Inc., Hatfield, PA, USA) to 15 mm × 30 mm brass plates and placed into a Quorum PP2000 cryopreparation chamber (Quorum Technologies, East Sussex, UK) attached to an S-4700 field emission scanning electron microscope (Hitachi High Technologies America, Inc., Dallas, TX, USA). The powder samples were placed directly into the scanning electron microscope at 5.0 kV, followed by sputter-coating with platinum.

2.4.7. Contact Angle. Contact angle measurement was performed by a sessile drop method using an Attention Theta optical tensiometer (Biolin Scientific, Linthicum Heights, MD, USA). The placement of droplets was controlled by a C201 automatic liquid dispenser (Biolin Scientific, Linthicum Heights, MD, USA). A 20 μL aliquot of pure DI water was dropped onto modified gold surfaces. Data collection (60 fps) was manually triggered by initial contact of a liquid drop with a solid surface. Captured images were automatically analyzed by One Attension software, version 1.8 (Biolin Scientific), to identify the baseline and calculate the contact angles.

2.5. Emulsion Preparation. An oil-in-water (O/W) emulsion was prepared as follows. The continuous phase was prepared by dissolving 0.2 g of UiO-66-NH_2 and virous polyethylene glycol (PEG, 10% w/w) in 30 mL of DI water by

vortexing at 3000 rpm. Different amounts of the dispersed phase (i.e., medium-chain triglycerides, MCTs) were added into the continuous phase. After that, the mixtures were sheared to form a coarse emulsion by using a high-speed homogenizer (Ultra-Turrax T25, IKA, Staufen, Germany) at 24,000 rpm for 5 min in an ice bath. The total mass of the system was 15 g,[26] with the composition shown in Table S1.

2.6. Characterization of UiO-66-NH_2 Pickering Emulsion. *2.6.1. Rheological Property.* The dynamic viscoelastic behavior of HIPPEs was characterized using a HAAKE RS600 Rheometer (HAAKE Co., Germany) with parallel plates (d = 27.83 mm) at 25 °C. The gap between the two plates was set to 1.0 mm. For the strain sweep mode, elastic (G') and loss moduli (G'') were recorded with the strain (γ) changing from 0.002 to 1.0 at a fixed frequency of 1.0 Hz. For the frequency sweep mode, the frequency oscillated from 0.1 to 10 Hz, and all measurements were performed at 0.5% strain, which was within the identified linear viscoelastic region.[27]

2.6.2. Low-Temperature Scanning Electron Microscopy (LT-SEM). Samples were scooped into a 10 mm cup and placed into a shuttle, which was frozen conductively in a Styrofoam box by placing the brass plates on the surface of a precooled (−196 °C) brass bar whose lower half was submerged in liquid nitrogen. After 20−30 s, the shuttle containing the frozen sample was transferred to a Quorum PP2000 cryopreparation chamber. The top layer of the frozen sample was cryofractured using a metal blade mounted inside the preparation chamber. All specimens were etched inside the cryopreparation system to remove any surface contamination (condensed water vapor) by raising the temperature of the stage to −90 °C for 10−15 min. Following the etching, the temperature inside the chamber was lowered below −130 °C, and the specimens were coated with a 10 nm layer of platinum using a magnetron sputter head equipped with a platinum target inside the cryopreparation chamber. The specimens were transferred to a precooled (−130 °C) cryostage in the scanning electron microscope for observation. An accelerating voltage of 5 kV was used to view the specimens. Images were captured using a 4pi Analysis system (Durham, NC).

2.6.3. Confocal Laser Scanning Microscopy (CLSM). A Zeiss LSM710 CLSM (Carl Zeiss Microscopy LLC, Thornwood, NY) system was utilized for the observation of the emulsion system. The images were obtained using a Zeiss Axio Observer inverted microscope with 10× 0.45 NA and 63× 1.4 NA Plan-Apochromat objectives. A 561 nm diode-pumped solid-state laser was used with a pin hole of 57 μm passing through an MBS 458/514 beam splitter filter with limits set between 540 and 750 nm. Zeiss Zen 2012 (Carl Zeiss Microscopy LLC, Thornwood, NY) software was used to obtain 7−21 z-stack images, and a maximum intensity projection was used to develop the final image.

2.6.4. Loading Capacity. To achieve high solubility, 1.5 g of curcumin was first added to 100 mL of MCT. Then, the mixture was treated with sonication (390 W, 15 min, 2 s interval, model 505, Fisherbrand, PA, USA). Afterward, the mixture was centrifuged for 2 min under 3000 rpm, and the supernatant was collected (10.02 mg/mL). All the collected solutions were kept at room temperature in the dark for 24 h before analysis. Aliquots of the curcumin oil solutions and Pickering emulsions were extracted and diluted for 1000 times with 95% alcohol for establishing a standard curve. The blank sample contained 95% alcohol without curcumin. The absorbance at a wavelength of 426 nm for the samples was
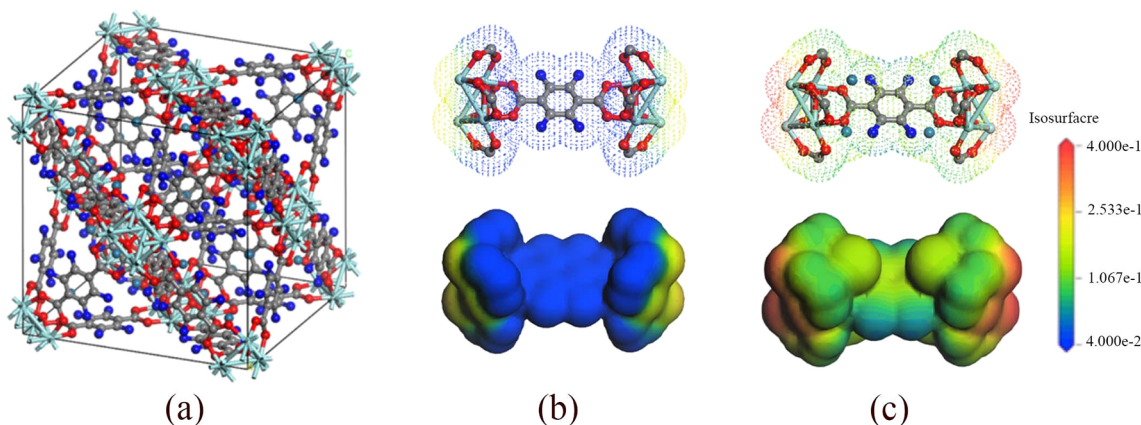
Figure 1. (a) Simulation view of the UiO-66 porous structure. Carbon: gray; oxygen: red; zirconium: blue-green. (b) Molecular electrostatic potential maps of UiO-66. (c) Molecular electrostatic potential maps of UiO-66-NH$_2$.
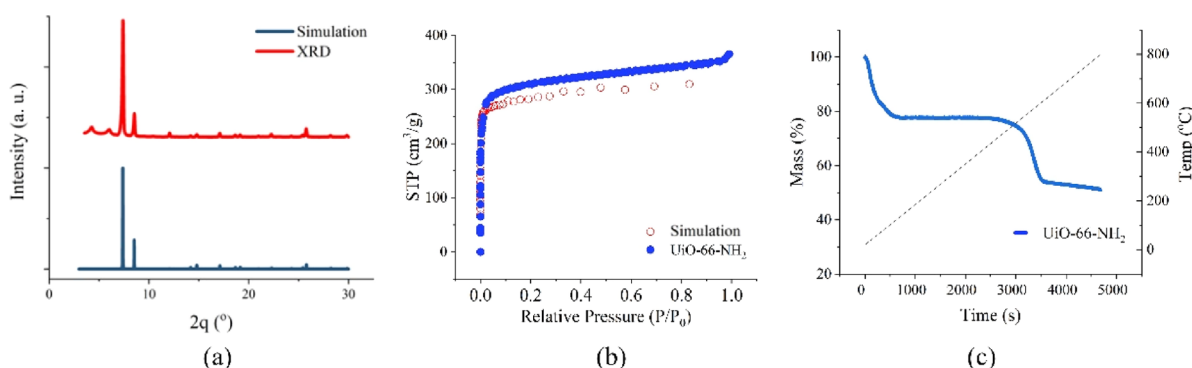

Figure 2. (a) PXRD patterns of UiO-66-NH$_2$. (b) N$_2$ adsorption isotherms at 77 K on UiO-66-NH$_2$. (c) Thermogravimetric analysis of UiO-66-NH$_2$.

determined using a UV spectrophotometer.[28] All determinations were performed in triplicate, and the curcumin content of each sample was calculated according to the standard curve (curcumin in ethanol, standard curve equation: $Y = 0.0146X + 0.0222$, $R^2 = 0.9993$).

The loading capacity (LC) was calculated using eq 3 for curcumin[29]

$$LC\% = \left(\frac{\text{weight of curcumin in emulsion system}}{\text{weight of total emulsion system}} \right) \times 100\%$$

(3)

The encapsulation efficiency (EE) was calculated using eq 4 for curcumin

$$EE\% = \left(\frac{\text{weight of curcumin in emulsion system}}{\text{weight of curcumin}} \right) \times 100\%$$

(4)

2.7. Statistical Analysis. Data on DLS, zeta-potential analysis, and LC measurements were collected from three true triplicates and were reported as the mean ± standard error. Data were analyzed by a one-way analysis of variance using the SPSS 16.0 package (SPSS Inc., Chicago, USA). The significance level was set at $p = 0.05$.

3. RESULTS AND DISCUSSION

3.1. Characterization of UiO-66-NH$_2$ Nanoparticles. The simulated structure of UiO-66 is shown in Figure 1a. The structure comprises Zr$_6$O$_4$(OH)$_4$ octahedrons (formed in situ

via hydrolysis of ZrCl$_4$) bridged by 1,4-benzene dicarboxylate (BDC) linkers. Each cationic Zr$_6$O$_4$(OH)$_4$ node is connected with 12 adjacent nodes by BDC linkers. The structure contains two sizes of cavities: an 11 Å octahedral cage and an 8 Å tetrahedral cage. Each large cage is sharing with eight small ones and edge-sharing with eight additional large ones. This unique structure leads to both high porosity and high stability. According to a previous study, UiO-66 can be modified by different functional groups at the ortho position of the benzene ring of BDC to generate derivatives such as UiO-66-OH, UiO-66-NH$_2$, and UiO-66-COOH, which would share the same crystal structure as UiO-66.[30]

It is expected that modification on UiO-66 with amino groups (−NH$_2$) would increase the electrostatic potential of the molecule surface so that UiO-66-NH$_2$ particles may be used as a stabilizer for Pickering emulsion systems. To test that hypothesis, we performed a DFT simulation comparison between UiO-66 and UiO-66-NH$_2$. According to previous reports, it is adequate to describe the intermolecular interactions of MOF by two Zr nodes and a single linked ligand, which provides a reasonable balance between accuracy and computational expense using the method in this work (PW91/DNP).[18] The molecular electrostatic potential of UiO-66 and UiO-66-NH$_2$ is shown in Figure 1b,c, respectively. The red area represents the place with the most positive electrostatic potential, whereas the blue area denotes the most negative part. It was found that after modification, the positive surface electrostatic potential increased significantly, possibly due to the change in the probability density of

electron clouds caused by $\pi-\pi$ interactions.[31] Moreover, the increased absolute value of the molecular electrostatic potential enhanced electrostatic repulsion between UiO-66-NH$_2$ particles, which may indicate a better stabilizing property for Pickering emulsion systems.

Subsequently, UiO-66 and UiO-66-NH$_2$ were synthesized by the solvothermal method using different BDC ligands (i.e., terephthalic acid and 2-aminoterephthalic acid) under the same condition. The comparison between the simulated and experimental XRD results of UiO-66-NH$_2$ showed that the characteristic peaks were nearly identical, which indicated that the crystal structure of the synthesized product was consistent with the expectation (Figure 2a).

Figure 2b illustrates comparisons between data from the simulation and experiment for N$_2$ absorption of UiO-66-NH$_2$ nanoparticles. The result from the simulation (1112 m^2/g) was in good agreement with the experimental data (1230 m^2/g). Moreover, the BET surface area obtained in this study was higher than those of other types of water-stable MOFs prepared by different metal ions and organic linkers, such as NU-1000 (617 m^2/g) and MIL-68 (584 m^2/g), but lower than HKUST-1 (1451 m^2/g).[32] Thereafter, through the computer simulation, we have obtained other physicochemical characteristics of UiO-66-NH$_2$, including molecular weight, density, accessible pore volume, etc. (Table 1).

Table 1. Computer Simulation Output of UiO-66-NH$_2$ Characteristics

property	simulation output
mass	8720.29 g/mol
density	1664.06 kg/m^3
accessible pore volume	0.41836 cm^3/g
gravimetric surface area (nitrogen)	1280.36 m^2/g
geometric surface area	1550.73 m^2/g
simulated BET surface area	1367.74 m^2/g
cavities	11 Å (large)
	8 Å (small)

The thermal stability of UiO-66-NH$_2$ was tested by TGA. Figure 2c shows two major weight loss stages for UiO-66-NH$_2$ nanoparticles. The first weight loss happened at a temperature range below 150 °C, which was contributed by the evaporation of immobilized free water from the crystal. Another weight loss happened at ca. 550 °C, which was ascribed to UiO-66-NH$_2$ lattice breakdown. These results were consistent with previous

reports, which further validated the structures of the synthesized MOF material.

As is evident, the particle size of the surfactant plays an essential role in the physicochemical properties of Pickering emulsions. As shown in Figure 3a, the average particle size of UiO-66-NH$_2$ was 161.4 nm with a polydispersity index (PDI) of 11.2, which indicated the excellent monodispersity and uniformity of the particles. Furthermore, scanning electron microscopy (SEM) was applied to measure the particle size and morphology after the sample was freeze-dried (Figure 3b). A representative SEM image showed that all particles shared a discoid morphology with a particle size in the range of 100–200 nm, which was consistent with the results from the DLS measurement. Meanwhile, UiO-66-NH$_2$ particles showed clear boundaries in the image, which was in agreement with previous reports.[8,30]

Particles adsorbed strongly to oil–water interfaces, and the energy of attachments depends on the water contact angle θ_{wca}. As shown in Figure 3c, the water contact angle (WCA) of UiO-66-NH$_2$ was stabilized approximately at 78 ± 2° for more than 10 s. At WCAs closer to 90°, the absorption energy of the particles to the interface of the droplet was closer to its maximum and the required energy to stabilize the Pickering emulsion system was at its minimum. In practice, particles with a WCA lower or higher than 90° were considered ideal for O/W or W/O Pickering emulsions, respectively.[12] Therefore, after modification with amino groups, UiO-66-NH$_2$ particles with a WCA of 78° were deemed suitable for stabilizing O/W Pickering emulsions as compared to some Pickering stabilizers that had a WCA as low as 73° in a previous report,[36] which was expected to reduce the surface tension and stabilize the emulsion.

In addition to the particle size and WCA, the electrostatic force was critical in determining the dispersibility of the particles in water and its ability to stabilize the Pickering emulsion.[33] The results on electrostatic potential calculated from the computer simulation have been discussed in Section 3.1. To further confirm this result, we measured the zeta potential of all treatments in different pH values (Figure 3a). The pH$_{pzc}$ (point of zero charges) value for UiO-66-NH$_2$ was ca. 4.0. Compared with other particles around 7.0 or above (e.g., protein, silica, and zeolite), UiO-66-NH$_2$ particles have a stronger positive surface charge at low pH values (up to 42 mV).

In summary, UiO-66-NH$_2$ particles have an acceptable amphiphilic property, proper electrostatic attraction, and
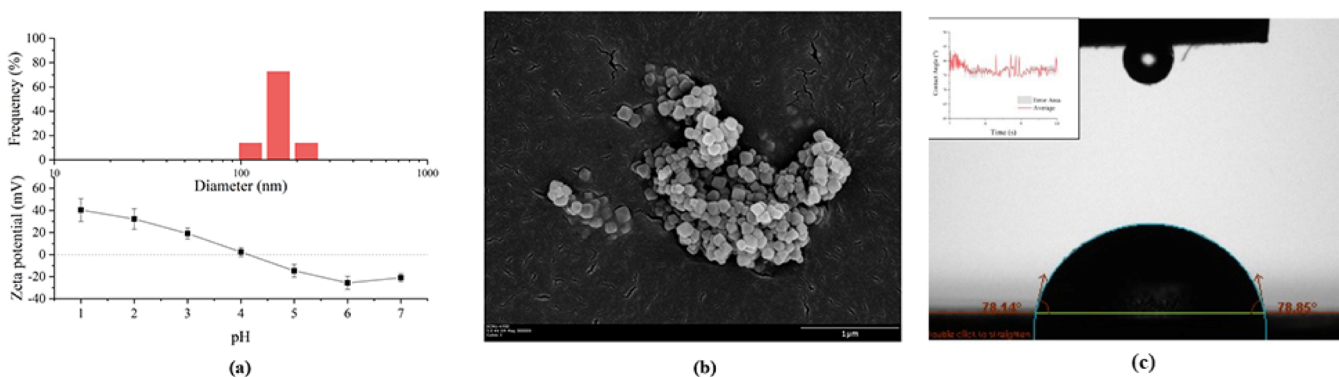

Figure 3. (a) Particle size distribution of UiO-66-NH$_2$ (top) and zeta potential of UiO-66-NH$_2$ at different pH values (bottom). (b) SEM images of UiO-66-NH$_2$. (c) WCA of UiO-66-NH$_2$.
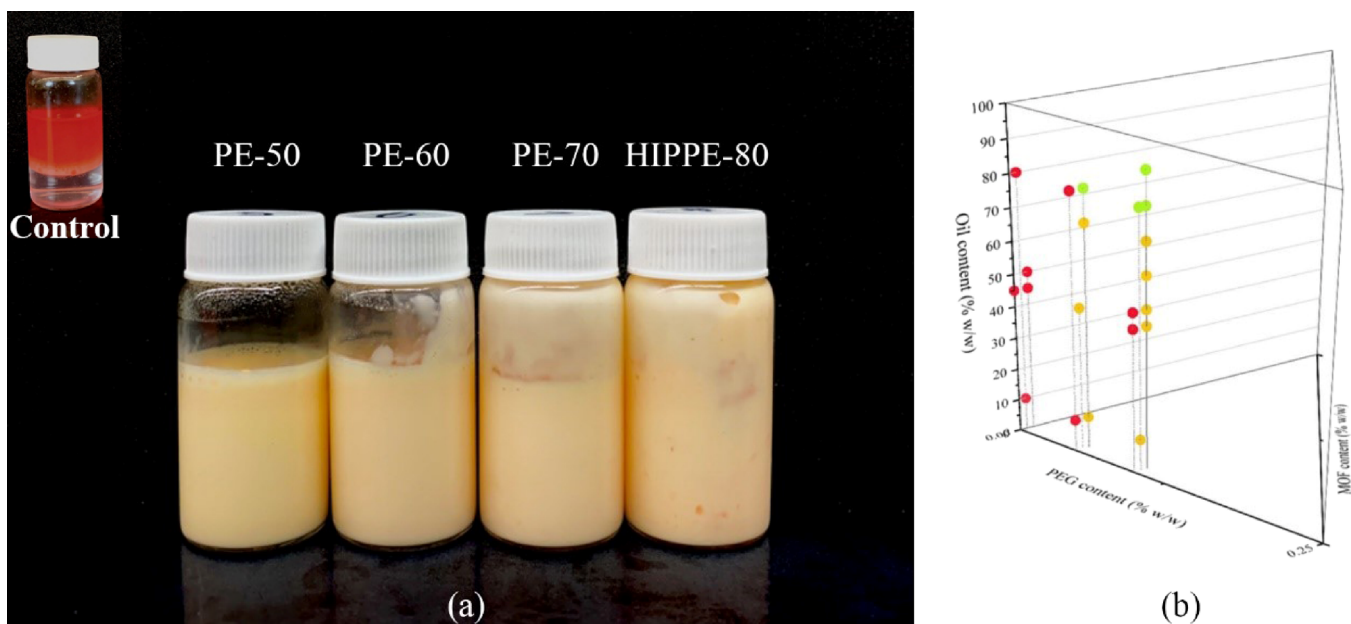
Figure 4. (a) Visual appearance of MOF-stabilized emulsions at different O:W ratios. (b) Stabilization of HIPPEs that contain various concentrations of PEG and UiO-66-NH$_2$ particles. Red dot: unstable emulsion; brown dots: emulsion only; green dots: HIPPE.
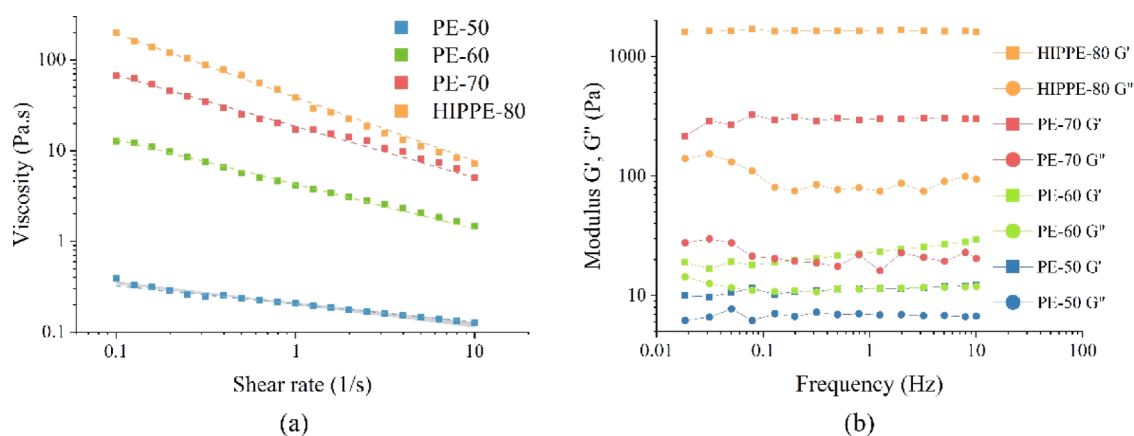

Figure 5. (a) Apparent viscosity of Pickering emulsions at different O:W ratios. (b) Storage modulus (G') and loss modulus (G'') as a function of angular frequency for the stabilized Pickering emulsions.

particle size, which contributed to reducing phase separation. Therefore, it is expected that UiO-66-NH$_2$ nanoparticles were feasible to stabilize the Pickering emulsion.

3.2. Pickering Emulsion Stabilized by UiO-66-NH$_2$. UiO-66-NH$_2$-stabilized Pickering emulsion was developed by in situ high-pressure homogenization with PEG as a depleter. Control experiments showed that without PEG, only Pickering emulsions with a low O:W ratio (less than 50%) was successfully obtained by homogenization. In contrast, with the absence of UiO-66-NH$_2$, PEG cannot be used alone as an emulsifier to stabilize the emulsion systems (see the control sample in Figure 4a). Here, the results showed that when MOF particles and PEG coexisted and exceeded 0.5 and 5% w/w, respectively, a Pickering emulsion was formed with one-step homogenization. The definition of a HIPPE was when the minimum volume ratio of an internal phase was higher than 0.74.[15] In this study, as shown in Figure 4b, a HIPPE (green dots) was obtained under the following two conditions: (1) PEG was at 0.5 to 5% w/w and UiO-66-NH$_2$ was higher than 1% w/w; (2) UiO-66-NH$_2$ was at 0.5 to 5% w/w and PEG was

higher than 10% w/w. When either of these two conditions was achieved, a HIPPE with a volume ratio of internal phase at up to 90% was successfully prepared.

For visual comparison, the emulsion was dyed by dissolving a fluorescent dye (Nile red) in the oil phase. Figure 4a shows the appearance of Pickering emulsions with the volume ratio of the internal phase at 50, 60, 70, and 80% (hereafter referred to as PE-50, PE-60, PE-70, and HIPPE-80, respectively) after 24 h of storage under ambient conditions. In the control sample (i.e., upper left image), the upper layer was MCT, in which the Nile red dye was dissolved, and the lower layer was a transparent aqueous phase, in which PEG was dissolved and obvious sedimentation and a clear water−oil separation were observed. However, different from unlike the control sample, all other Pickering emulsions remained homogenized. The disappearance of the apparent red color proved that the oil phase was successfully encapsulated in the emulsion systems. The different amounts of wall-mounted emulsion after storage indicated that the mobility of the emulsion was different.

To better understand the stabilization mechanism, the rheological properties of Pickering emulsions were investigated. For all Pickering emulsions, the apparent viscosity (η) gradually decreased with an increase in the shear rate from 0.1 to 10 s^{-1}, indicating the shear-thinning behavior of all emulsions. As pointed by Wei et al., the Pickering emulsion system is a type of power-law fluid that follows Ostwald−de Waele's relationship.[27] The apparent viscosity η is given by eq 5

$$\eta_{app} = K \left(\frac{\partial u}{\partial y} \right)^{n-1}$$
(5)

where K is the flow consistency index in Pa s^n, $\frac{\partial u}{\partial y}$ is the shear rate or velocity gradient perpendicular to the plane of shear in s^{-1}, and n is the flow behavior index (dimensionless). The experimental data were successfully fitted to the model (Figure 5), and the K value and flow behavior index of the four Pickering emulsions are calculated and presented in Table S1. It can be found that for the MOF−Pickering emulsions, the flow behavior index was always less than 1, which indicated that these emulsion systems were pseudoplastic fluids. At the same time, the value of n decreased with increasing O:W ratio. One plausible explanation was that for both normal Pickering emulsion and HIPPE, UiO-66-NH$_2$ particles generated a concentrated form, which means that even under low inner phase conditions, particle-filled weak gels were formed within the system. With the increase in dispersion phase concentration, the network of aggregated droplets, which contain a long-chain polymer (PEG) at a high O:W ratio, endowed the system with high viscosity.[9] This hypothesis is also supported by the flow consistency index (K). The K value increased significantly as the oil content increased (e.g., K = 4.3, 18.5, and 38.8 for PE-60, PE-70, and HIPPE-80, respectively) (Table S1), suggesting a dramatic increase in viscosity.

Dynamic oscillatory data with different O:W ratios are shown in Figure 5b. With increasing angular frequency, neither shear storage nor shear loss modulus changed significantly. The damping ability of a system (i.e., the ratio of the storage modulus to the loss modulus, tan δ) decreases significantly with increasing O:W ratio. In addition, the sample with a higher O:W ratio showed a smaller tan δ value, which could be attributed to the fact that the loss modulus was lower than its storage modulus in the HIPPE system. As shown in Figure 5b, the damping ability decreased rapidly as the O:W ratio increased from 60 to 70% w/w. Moreover, after the formation of the HIPPE system, the value of tan δ decreased far from 1, which suggested increased pseudoelasticity. It is worth noting that previous reports suggest that viscosity does not play a predominant role in stabilizing the HIPPE system.[16] Combining the previous discussion of emulsion viscosity, at the relatively low ratio of O:W (<60% w/w), viscosity was essential for emulsion stability. However, with the increase in emulsion O:W ratio, especially from 60 to 70% w/w, the interaction between droplets in the system rapidly increased, and the effect of viscosity on emulsion stability was significantly reduced.

Studies have demonstrated that the HIPPE system was a bridging hydrogel network, in which the droplet interface was a monolayer between droplets. The result was confirmed by the LT-SEM result, in which the diameter of droplets was around 10 μm (Figure 6). In general, the jamming packing effect was
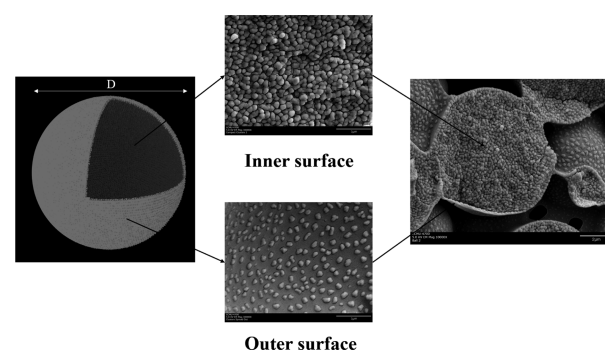

Figure 6. SEM images of MOF-HIPPE droplets with the theoretical model. The left figure shows the theoretical Pickering droplet model, and the right figure is an image from SEM. The upper middle image shows the droplet interface from the internal view, and the lower middle image shows the droplet interface from the outer view.

proportional to the effective volume fraction and the ratio of interface thickness to droplet size. Since the ratio of interface thickness to droplet size was less than 5%, the enhanced jamming packing due to the increase in the effective volume fraction would be negligible under this condition. Therefore, one possible explanation was that in the process of the system changing from a Pickering emulsion system to a HIPPE, the depletion interaction brought by PEG plays a vital role in the process of stabilizing the system to overcome the phase inversion of the emulsion.[9]

Depletion interaction is a type of physical interaction that facilitates hydrophilic particle absorption to the droplet interface, which is induced by the presence of cosolvents.[9,37] When both large UiO-66-NH$_2$ particles and small PEG depletants were in a suspension, the region that surrounds every large MOF particle was unavailable for the centers of the PEG to occupy. During the homogenization process, although depletion attraction tends to flocculate the particles, when the two particles are close enough, the strong repulsive interaction between the particles helps particles stay individually (calculated from the DLVO model). At the same time, due to the strong external force in the system during the homogenization, the UiO-66-NH$_2$ particles tend to stabilize on the surface of the oil droplet, thus reducing the surface tension.

To investigate the changes in the interface during the formation of HIPPE, we took confocal microscopy images of representative regimes from PE-60, PE-70, and HIPPE-80 and named them regime-1, regime-2, and regime-3, respectively (Figure 7). In the case of regime-1, which denotes a low internal phase, the distance between the adjacent droplets in the system was large, and the exclusion volume was formed by the electrostatic force and van der Waals force outside the droplets. The droplet motion under this condition was mainly affected by the viscosity of the continuous phase. With the increase in O:W ratio, the volume of nonexclusion volume areas in some parts of the system decreased, and the overlap of the exclusion volume began to occur near the interface of the adjacent droplets, which became regime-2. In this region, due to the effect of depletion attraction brought by PEG, MOF particles were stabilized at the interface. Therefore, phase inversion would not happen. As the amount of oil phase increases continuously, the contact area between the two interfaces merges to form a monoisolation layer. Eventually, any two adjacent droplets in the system were forced to form a
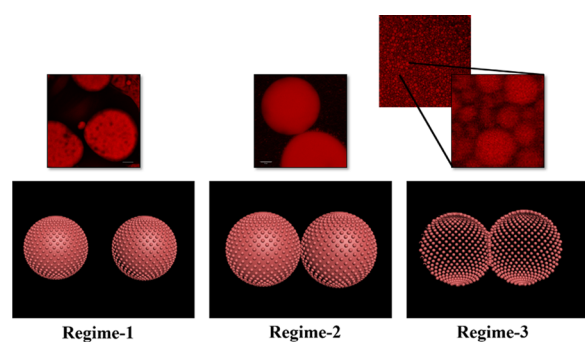
Figure 7. Representative confocal laser scanning microscopy (CLSM) images of the HIPPE in different regimes. The upper three images were imaged by CLSM from the representative regime, and the lower three images were mapped to their theoretical model.

tightly packed emulsion structure, leading to the formation of regime-3. In this regime, droplets were surrounded by the MOF particle layer, which stabilizes the emulsion mechanically and prevents sedimentation.

3.3. Loading Capacity of the MOF-HIPPE System. The HIPPE emulsion system was prepared under the O:W ratio higher than 80% w/w, which suggests the possibility of a high payload of oil-soluble compounds such as curcumin. In principle, the loading capacity (LC) and encapsulation efficiency (EE) of curcumin were positively related to the O:W ratio of the Pickering emulsion system. The LC of curcumin in the UiO-66-NH$_2$-stabilized HIPPE was measured at 6.93 ± 0.41%, and the EE of the system was 19.76 ± 3.84%, significantly higher than the conventional Pickering emulsion systems (i.e., PE-70 and PE-80). When compared to other emulsion systems, the loading capacity was relatively low, which may be due to the amphiphilicity of the UiO-66-NH$_2$ NPs. As mentioned before, the WCA of UiO-66-NH$_2$ NPs was 78°, which indicated that they were more hydrophobic than other stabilizers, e.g., protein and silica dioxide. The EE showed a significant correlation to the WCA. When the WCA was closer to 90°, the system would show a higher EE (see Section 3.1).

At present, one of the main disadvantages of the Pickering emulsion system for food application was low LC and EE. As expected, compared with protein-stabilized traditional Pickering emulsions, the MOF-HIPPE system showed a higher loading capacity. For example, the LC values were 0.0016 wt %[34] for the octenyl succinic anhydride (OSA) quinoa starch Pickering emulsion and 0.0005 wt % for the kafirin Pickering emulsion[35] with in situ homogenization. The high LC and EE values of the MOF-HIPPE system can be attributed to two reasons below: (a) the high internal phase system could load more dispersed phases with dissolved saturated curcumin due to the high water−oil ratio, and (b) the MOF particles were highly porous materials, so the particles themselves provided the loading capacity, and therefore, the loading was further increased. In summary, as we selected a water-stable and high-bioaffinity MOF material, this shed light on further expansion of novel reticular materials for food applications in the future.

4. CONCLUSIONS

In this study, for the first time, with the help of computational simulation, we have established a hydrophobic bioactive compound-loaded MOF-HIPPE system. With the assistance of simulated computation, UiO-66-NH$_2$ was optimized for stabilizing O/W Pickering emulsions due to its evenly distributed positive surface potential and amphiphilic properties. The solvothermal method was applied for the facile synthesis of monodisperse UiO-66-NH$_2$ particles with the particle size of 161.36 nm. Experimental results on the crystal structure by XRD, porosity by BET, particle size and zeta potential by DLS, and morphology by SEM showed high consistency with simulation expectations. Pickering emulsion systems with different contents of MOF particles and PEG and O:W ratios were prepared by in situ homogenization. Afterward, rheological and morphological studies demonstrated that increasing the viscosity of the continuous phase and enhancing depletion attraction helped stabilize the Pickering emulsions and prevent phase inversion as the internal phase ratio increased. Finally, curcumin was encapsulated into the newly prepared MOF-HIPPE system and achieved a higher LC and EE compared with other food Pickering emulsion delivery systems, up to 6.93 ± 0.41% for LC and 19.76 ± 3.84% for EE. This UiO-66-NH$_2$-stabilized HIPPE system was a successful example to develop other MOF-HIPPE systems, and a similar strategy may be useful to create more hierarchical structures based on novel highly porous materials for food applications. The next step, the effect of a single factor, the stability and toxicology of the system, and application in the food industry need to be explored.

■ ASSOCIATED CONTENT

ⓢ Supporting Information

The Supporting Information is available free of charge at https://pubs.acs.org/doi/10.1021/acsomega.1c03932.

> Table S1: three-factor Box−Behnken design for the MOF-HIPPE system; Table S2: fitting results of emulsion rheology analysis based on the Ostwald−de Waele model; Figure S1: approximate-calculation schematic of a UiO-66-NH$_2$ particle; Figure S2: 3D cross-sectional geometry of the overlapping volume where the green balls represent PEG in the continuous phase (PDF)

■ AUTHOR INFORMATION

Corresponding Author

    Qin Wang − *Department of Nutrition and Food Science, College of Agriculture and Natural Resources, University of Maryland, College Park, Maryland 20742, United States;* ⓞ orcid.org/0000-0002-7496-3921; Phone: 301-405-8421; Email: wangqin@umd.edu

Authors

    Peihua Ma − *Department of Nutrition and Food Science, College of Agriculture and Natural Resources, University of Maryland, College Park, Maryland 20742, United States*

    Jinglin Zhang − *Department of Nutrition and Food Science, College of Agriculture and Natural Resources, University of Maryland, College Park, Maryland 20742, United States;* ⓞ orcid.org/0000-0002-5058-9488

    Zi Teng − *Department of Nutrition and Food Science, College of Agriculture and Natural Resources, University of Maryland, College Park, Maryland 20742, United States; Agricultural Research Service, Beltsville Agricultural Research Center, Food Quality Laboratory, U.S. Department of Agriculture, Beltsville, Maryland 20705, United States;* ⓞ orcid.org/0000-0002-6029-7024

Yuan Zhang − *Department of Chemistry and Biochemistry, College of Computer, Mathematical and Natural Science, University of Maryland, College Park, Maryland 20742, United States*

Gary R. Bauchan − *Agricultural Research Service, Soybean Genomics and Improvement Laboratory, Electron and Confocal Microscopy Unit, U.S. Department of Agriculture, Beltsville, Maryland 20705, United States*

Yaguang Luo − *Agricultural Research Service, Beltsville Agricultural Research Center, Food Quality Laboratory, U.S. Department of Agriculture, Beltsville, Maryland 20705, United States*

Dongxia Liu − *Department of Chemistry and Biochemistry, College of Computer, Mathematical and Natural Science, University of Maryland, College Park, Maryland 20742, United States;* ⬤ orcid.org/0000-0001-8712-2219

Complete contact information is available at:
https://pubs.acs.org/10.1021/acsomega.1c03932

Notes

The authors declare no competing financial interest.

■ ACKNOWLEDGMENTS

■ REFERENCES

(1) Horcajada, P.; Chalati, T.; Serre, C.; Gillet, B.; Sebrie, C.; Baati, T.; Eubank, J. F.; Heurtaux, D.; Clayette, P.; Kreuz, C.; Chang, J.-S.; Hwang, Y. K.; Marsaud, V.; Bories, P.-N.; Cynober, L.; Gil, S.; Feŕey, G.; Couvreur, P.; Gref, R. Porous metal-organic-framework nanoscale carriers as a potential platform for drug delivery and imaging. *Nat. Mater.* **2010**, *9*, 172−178.

(2) Moghadam, P. Z.; Li, A.; Wiggin, S. B.; Tao, A.; Maloney, A. G. P.; Wood, P. A.; Ward, S. C.; Fairen-Jimenez, D. Development of a Cambridge Structural Database Subset: A Collection of Metal-Organic Frameworks for Past, Present, and Future. *Chem. Mater.* **2017**, *29*, 2618−2625.

(3) Gangu, K. K.; Maddila, S.; Mukkamala, S. B.; Jonnalagadda, S. B. A review on contemporary Metal−Organic Framework materials. *Inorg. Chim. Acta* **2016**, *446*, 61−74.

(4) Jarai, B. M.; Stillman, Z.; Attia, L.; Decker, G. E.; Bloch, E. D.; Fromen, C. A. Evaluating UiO-66 Metal−Organic Framework Nanoparticles as Acid-Sensitive Carriers for Pulmonary Drug Delivery Applications. *ACS Appl. Mater. Interfaces* **2020**, *12*, 38989−39004.

(5) Gandara-Loe, J.; Ortuño-Lizarán, I.; Fernández-Sanchez, L.; Alió, J. L.; Cuenca, N.; Vega-Estrada, A.; Silvestre-Albero, J. Metal−organic frameworks as drug delivery platforms for ocular therapeutics. *ACS Appl. Mater. Interfaces* **2019**, *11*, 1924−1931.

(6) Su, F.; Jia, Q.; Li, Z.; Wang, M.; He, L.; Peng, D.; Song, Y.; Zhang, Z.; Fang, S. Aptamer-templated silver nanoclusters embedded in zirconium metal−organic framework for targeted antitumor drug delivery. *Microporous Mesoporous Mater.* **2019**, *275*, 152−162.

(7) Qiu, C.; McClements, D. J.; Jin, Z.; Qin, Y.; Hu, Y.; Xu, X.; Wang, J. Resveratrol-loaded core-shell nanostructured delivery systems: Cyclodextrin-based metal-organic nanocapsules prepared by ionic gelation. *Food Chem.* **2020**, *317*, 126328.

(8) Ma, P.; Zhang, J.; Liu, P.; Wang, Q.; Zhang, Y.; Song, K.; Li, R.; Shen, L. Computer-assisted design for stable and porous metal-organic framework (MOF) as a carrier for curcumin delivery. *LWT* **2020**, *120*, 108949.

(9) Kim, K.; Kim, S.; Ryu, J.; Jeon, J.; Jang, S.; Kim, H.; Gweon, D.; Im, W.; Han, Y.; Choi, S. Processable high internal phase Pickering emulsions using depletion attraction. *Nat. Commun.* **2017**, *8*, 14305.

(10) Tikekar, R. V.; Pan, Y.; Nitin, N. Fate of curcumin encapsulated in silica nanoparticle stabilized Pickering emulsion during storage and simulated digestion. *Food Res. Int.* **2013**, *51*, 370−377.

(11) Xiao, J.; Lu, X.; Huang, Q. Double emulsion derived from kafirin nanoparticles stabilized Pickering emulsion: Fabrication, microstructure, stability and in vitro digestion profile. *Food Hydrocolloids* **2017**, *62*, 230−238.

(12) McClements, D. Enhanced delivery of lipophilic bioactives using emulsions: a review of major factors affecting vitamin, nutraceutical, and lipid bioaccessibility. *Food Funct.* **2018**, *9*, 22−41.

(13) Cai, D.; Thijssen, J. H. T.; Clegg, P. S. Making non-aqueous high internal phase pickering emulsions: influence of added polymer and selective drying. *ACS Appl. Mater. Interfaces* **2014**, *6*, 9214−9219.

(14) Lissant, K. The geometry of high-internal-phase-ratio emulsions. *J. Colloid Interface Sci.* **1966**, *22*, 462−468.

(15) Ikem, V. O.; Menner, A.; Bismarck, A. High Internal Phase Emulsions Stabilized Solely by Functionalized Silica Particles. *Angew. Chem., Int. Ed.* **2008**, *47*, 8277−8279.

(16) Xu, Y.-T.; Tang, C.-H.; Liu, T.-X.; Liu, R. Ovalbumin as an Outstanding Pickering Nanostabilizer for High Internal Phase Emulsions. *J. Agric. Food Chem.* **2018**, *66*, 8795−8804.

(17) Menner, A.; Ikem, V.; Salgueiro, M.; Shaffer, M.; Bismarck, A. High internal phase emulsion templates solely stabilised by functionalised titania nanoparticles. *Chem. Commun.* **2007**, *6*, 4274−4276.

(18) Liu, Y.; Liu, J.; Chang, M.; Zheng, C. Theoretical studies of CO2 adsorption mechanism on linkers of metal-organic frameworks. *Fuel* **2012**, *95*, 521−527.

(19) Dubbeldam, D.; Calero, S.; Ellis, D. E.; Snurr, R. Q. RASPA: molecular simulation software for adsorption and diffusion in flexible nanoporous materials. *Mol. Simul.* **2016**, *42*, 81−101.

(20) Miklitz, M.; Jelfs, K. E. pywindow: Automated Structural Analysis of Molecular Pores. *J. Chem. Inf. Model.* **2018**, *58*, 2387−2391.

(21) Bernini, M. C.; Fairen-Jimenez, D.; Pasinetti, M.; Ramirez-Pastor, A. J.; Snurr, R. Q. Screening of bio-compatible metal-organic frameworks as potential drug carriers using Monte Carlo simulations. *J. Mater. Chem. B* **2014**, *2*, 766−774.

(22) Chen, Q.; He, Q.; Lv, M.; Xu, Y.; Yang, H.; Liu, X.; Wei, F. Selective adsorption of cationic dyes by UiO-66-NH2. *Appl. Surf. Sci.* **2015**, *327*, 77−85.

(23) Su, H.; Sun, F.; Jia, J.; He, H.; Wang, A.; Zhu, G. A highly porous medical metal-organic framework constructed from bioactive curcumin. *Chem. Commun.* **2015**, *51*, 5774−5777.

(24) Oh, S. C.; Wu, Y.; Tran, D. T.; Lee, I. C.; Lei, Y.; Liu, D. Influences of cation and anion substitutions on oxidative coupling of methane over hydroxyapatite catalysts. *Fuel* **2016**, *167*, 208−217.

(25) Zhang, J.; Mei, L.; Chen, N.; Yuan, Y.; Zeng, Q.-Z.; Wang, Q. Study on β-lactoglobulin microgels adsorption onto a hydrophobic solid surface by QCM-D. *Food Hydrocolloids* **2020**, *98*, 105320.

(26) Wei, Y.; Sun, C.; Dai, L.; Mao, L.; Yuan, F.; Gao, Y. Novel Bilayer Emulsions Costabilized by Zein Colloidal Particles and Propylene Glycol Alginate, Part 1: Fabrication and Characterization. *J. Agric. Food Chem.* **2019**, *67*, 1197−1208.

(27) Wei, Y.; Sun, C.; Dai, L.; Mao, L.; Yuan, F.; Gao, Y. Novel Bilayer Emulsions Costabilized by Zein Colloidal Particles and Propylene Glycol Alginate. 2. Influence of Environmental Stresses on Stability and Rheological Properties. *J. Agric. Food Chem.* **2019**, *67*, 1209−1221.

(28) Ma, P.; Zeng, Q.; Tai, K.; He, X.; Yao, Y.; Hong, X.; Yuan, F. Development of stable curcumin nanoemulsions: effects of emulsifier type and surfactant-to-oil ratios. *J. Food Sci. Technol.* **2018**, *55*, 3485−3497.

(29) Wei, Z.; Wang, C.; Liu, H.; Zou, S.; Tong, Z. Halloysite nanotubes as particulate emulsifier: Preparation of biocompatible drug-carrying PLGA microspheres based on pickering emulsion. *J. Appl. Polym. Sci.* **2012**, *125*, E358−E368.

(30) Katz, M. J.; Brown, Z. J.; Colon, Y. J.; Siu, P. W.; Scheidt, K. A.; Snurr, R. Q.; Hupp, J. T.; Farha, O. K. A facile synthesis of UiO-66, UiO-67 and their derivatives. *Chem. Commun.* **2013**, *49*, 9449−9451.

(31) Li, J.; Wu, Q.; Wang, X.; Chai, Z.; Shi, W.; Hou, J.; Hayat, T.; Alsaedi, A.; Wang, X. Heteroaggregation behavior of graphene oxide on Zr-based metal-organic frameworks in aqueous solutions: a combined experimental and theoretical study. *J. Mater. Chem. A* **2017**, *5*, 20398−20406.

(32) Wu, M.-X.; Yang, Y.-W. Metal-Organic Framework (MOF)-Based Drug/Cargo Delivery and Cancer Therapy. *Adv. Mater.* **2017**, *29*, 1606134.

(33) Boire, A.; Renard, D.; Bouchoux, A.; Pezennec, S.; Croguennec, T.; Lechevalier, V.; Le Floch-Fouéré, C.; Bouhallab, S.; Menut, P.; Doyle, M.; McClements, D. Soft-Matter Approaches for Controlling Food Protein Interactions and Assembly. *Annu. Rev. Food Sci. Technol.* **2019**, *10*, 521−539.

(34) Marefati, A.; Bertrand, M.; Sjoo, M.; Dejmek, P.; Rayner, M. Storage and digestion stability of encapsulated curcumin in emulsions based on starch granule Pickering stabilization. *Food Hydrocolloids* **2017**, *63*, 309−320.

(35) Xiao, J.; Lo, C.; Huang, Q. Kafirin Nanoparticle-Stabilized Pickering Emulsions as Oral Delivery Vehicles: Physicochemical Stability and in Vitro Digestion Profile. *J. Agric. Food Chem.* **2015**, *63*, 10263−10270.

(36) Ojala, J.; Visanko, M.; Laitinen, O.; Österberg, M.; Sirviö, J. A.; Liimatainen, H. Emulsion Stabilization with Functionalized Cellulose Nanoparticles Fabricated Using Deep Eutectic Solvents. *Molecules* **2018**, *23*, 2765.

(37) Hinrichs, D.; Himstedt, R.; Dorfs, D. The size-selective interaction of key and lock nanocrystals driven by depletion attraction at the nanoscale. *Nanoscale* **2018**, *10*, 9899.